Journal of Materials Chemistry A

ROYAL SOCIETY OF CHEMISTRY

PAPER

View Article Online
View Journal | View Issue

Cite this: J. Mater. Chem. A, 2025, 13, 17489

NHC–Ni nanoclusters covalently ligated on carbon nanotubes: highly active electrocatalysts for the oxygen evolution reaction†‡

Amalia Rapakousiou, *[a] Savvas G. Chalkidis,[b] Michail P. Minadakis,[a] María Luisa Ruiz-González,[c] Cristina Navio,[d] Georgios C. Vougioukalakis *[b] and Nikos Tagmatarchis *[a]

Developing robust and efficient oxygen evolution reaction (OER) electrocatalysts is essential for advancing renewable energy technologies like water electrolysis. Here, we present an electrocatalyst comprising N-heterocyclic carbene (NHC)-ligated nickel nanoclusters (NiNCs) covalently anchored on multi-walled carbon nanotubes (MWCNTs), with only 3.9% Ni/C atomic content. The unique nanoarchitecture, featuring a conductive NHC–Ni(0) core and an electroactive NiO_x shell, was prepared *via* a dual metal-reduction and transmetalation strategy, offering exceptional electrocatalytic stability and efficiency, whereas MWCNTs offer mechanical robustness and a conductive nanocarrier support contributing to the enhanced OER kinetics. The electrocatalyst demonstrates low overpotentials of 320 mV and 500 mV at 10 mA cm^{-2} and 200 mA cm^{-2}, respectively, in 1 M KOH, with very high specific (j_{ECSA} = 133 mA cm^{-2}) and intrinsic (j_{nNi} = 2.8 × 10^9 mA mol^{-1} cm^2) activities, as well as exceptional turnover frequencies (TOFs), reaching up to 7.4 s^{-1} under industrially relevant conditions (200 mA cm^{-2}). Electrochemical impedance spectroscopy reveals rapid charge transfer kinetics (R_{ct}: 66 Ω to 9.7 Ω) and efficient interfacial processes, driven by high dispersion and ultrafine NiNC size (<1.6 nm). The synergistic interplay between the NHC–Ni(0) core, which stabilizes the electroactive shell structure, and the MWCNTs, which enhance electron transport and provide mechanical robustness, ensures durability under prolonged cycling, with minimal losses (<1.3% overpotential gain and <0.5% apparent loss of Ni active sites). These results establish MWCNTs-NHC-ligated NiNCs as a scalable and high-performing electrocatalyst, surpassing RuO_2 and competitive NiFe-based materials, highlighting how precise nanoengineering through innovative covalent architecture can enable efficient and durable OER technologies in clean energy systems.

Received 28th January 2025
Accepted 26th April 2025

DOI: 10.1039/d5ta00780a

rsc.li/materials-a

Introduction

The Oxygen Evolution Reaction (OER) stands as a fundamental anodic process in electrochemical water splitting, essential for renewable energy technologies like water electrolysis and fuel cells.[1–5] Efficient electrocatalysts for the OER are crucial for advancing these technologies and enabling the production of clean and sustainable energy. Nickel-based materials, including nanoclusters and nanoparticles, have attracted considerable attention due to their abundance, cost-effectiveness, and promising electrocatalytic activity in the OER.[6–10] However, enhancing the performance and stability of nickel-based electrocatalysts remains a significant challenge.[11] Recent research is increasingly focusing on novel catalyst–support interactions to enhance the electrochemical performance of Ni-based nanomaterials.[12–16] In this context, exploring N-Heterocyclic Carbenes (NHCs) ligated to metal nanomaterials as electrocatalysts for the OER presents an underexplored but intriguing

[a]Theoretical and Physical Chemistry Institute, National Hellenic Research Foundation, 48 Vassileos Constantinou Avenue, Athens 11635, Greece. E-mail: arapak@eie.gr; tagmatar@eie.gr

[b]Laboratory of Organic Chemistry, Department of Chemistry, National and Kapodistrian University of Athens, Athens, 15771, Greece. E-mail: vougiouk@chem.uoa.gr

[c]Departamento de Química Inorgánica, Universidad Complutense de Madrid, Madrid, Spain

[d]IMDEA Nanoscience, Ciudad Universitaria de Cantoblanco, C/Faraday, 928049 Madrid, Spain

† Dedicated to Prof. Petra Rudolf on the occasion of her retirement, in profound appreciation of her outstanding contributions to science, her steadfast advocacy for women in research, and her enduring support and encouragement.

‡ Electronic supplementary information (ESI) available: Methods and full experimental procedures, schemes and data, ^1H, ^{13}C, ^{19}F and 2D NMR spectra, FTIR and ATR-FTIR spectra, Raman spectra and spectral maps, XPS spectra, TGA graphs, HAADF-STEM images and EDS maps, extensive electrochemical and electrocatalytic data, and comparative performance metrics. See DOI: https://doi.org/10.1039/d5ta00780a

avenue for innovation.[17–19] Among others, NHCs have emerged as promising ligands for tailoring the surface chemistry of metal nanomaterials.[20] Renowned for their strong metal-binding affinity and tunable electronic properties, NHCs offer the potential to modulate the catalytic activity and stability of nickel nanoclusters and nanoparticles.[21–23] Despite these promising attributes, the application of nanoscaled NHC–Ni interactions in electrocatalysis remains largely unexplored. This study aims to bridge this gap by investigating nanostructured MWCNTs-NHC-functionalized nickel nanoclusters (NiNCs) as electrocatalysts for the OER. Our nanoengineering strategy demonstrates the potential of rational nanoscale design in overcoming intrinsic material limitations to advance sustainable energy technologies.

In this work, we present a highly innovative electrocatalyst for the Oxygen Evolution Reaction (OER), featuring NHC-ligated NiNCs chemically bonded on oxidized Multi-Walled Carbon Nanotubes (oMWCNTs). The oMWCNTs, known for their inherent electrocatalytic properties, pose a significant challenge as a nanocarrier due to their already high baseline activity.[24] The synergistic interaction between NHC ligation, NiNCs, and MWCNT nanocarriers, however, achieves remarkable stability and electrocatalytic performance in the OER, outperforming oMWCNTs and surpassing the benchmark RuO_2 electrocatalyst.

Results and discussion

The implementation of NHC ligands to stabilize and enhance the catalytic activity of metal catalysts has been extensively explored, leading to the development of robust catalytic protocols.[25–27] In this regard, the synthetic strategy starts with the synthesis of an NHC-precursor ligand containing an alkyne group.[28] Next, a copper-catalyzed azide–alkyne cycloaddition (CuAAC) with 4-azidoaniline **4** yields NHC-precursor **5**, containing a 4-triazolylaniline group (Scheme 1, pages S5–S7 and Fig. S1–S11‡). The formation of NHC–Cu(I) complex **6** is achieved using a weak base route as outlined by Nolan's group,[29] with mesityl substituents providing steric protection and stability to the *in situ* generated NHC ligands and the resulting copper complex (Scheme 1, page S8 and Fig. S12–S14‡).

In parallel, pristine MWCNTs **7** were thoroughly purified to remove any residual metals (page S17 and Fig. S15–S17‡),[30] before undergoing oxidation in a 3 : 1 v/v H_2SO_4 : HNO_3 mixture, resulting in oMWCNTs **8** bearing carboxylic acid groups (Scheme S1, page S19 and Fig. S18–S21‡).[31] Nanomaterial **9** was then prepared *via* an amidation reaction between **8** and NHC–Cu(I) complex **6**, (page S22 and Fig. S22–S26‡). The coordination of Ni(II) was achieved by reacting **9** with hexahydrate nickel chloride, facilitated by both triazolyl and amide coordinating functionalities.[32,33] *In situ* reduction of Ni(II), transmetallation of NHC–Cu(I) to NHC–Ni(0) and subsequent nucleation of NiNCs in a water/ethanol mixture at room temperature, using sodium borohydride ($NaBH_4$) as the reducing agent, yielded the targeted electrocatalyst **10** (Scheme 2, page S26 and Fig. S27–S30‡).

Raman spectroscopy of MWCNTs **7** reveals an I_D/I_G ratio of 0.80 ± 0.01, with D and G bands at 1348 cm^{-1} and 1577 cm^{-1}, respectively, indicating the graphitic structure (Fig. S15–S16 and Table S1‡).[34,35] Upon oxidation to **8**, the I_D/I_G ratio increases to 1.03 ± 0.01, accompanied by D and G band peaks blue-shifting to 1355 cm^{-1} and 1587 cm^{-1}, confirming covalent surface functionalization (Fig. S18–S19 and Table S1‡).[36,37] ATR-FTIR analysis shows a carbonyl stretch at 1702 cm^{-1}, corresponding to –COOH groups (Fig. S20‡). TGA reveals a 6.5% weight loss at 600 °C, consistent with one –COOH group per 54 carbon atoms (Fig. S21‡).[38]

After amidation of **8**, with complex **6**, to form **9**, the Raman I_D/I_G ratio remains unchanged, suggesting that functionalization occurs primarily on the ligand chain without altering the MWCNT framework. Notably, small shifts of the D (1353 cm^{-1}) and G (1583 cm^{-1}) bands reflect changes in the electronic properties of the carbon framework (Fig. S22–S23 and Table S1‡).[39,40] ATR-FTIR shows an amide carbonyl stretching vibration at 1715 cm^{-1}, confirming successful modification (Fig. S24‡), while TGA suggests a ligand-to-carbon ratio of 1 : 79, consistent with sole "on-ligand" modification (Fig. S25‡). XPS analysis confirms the targeted nanostructure, with the survey

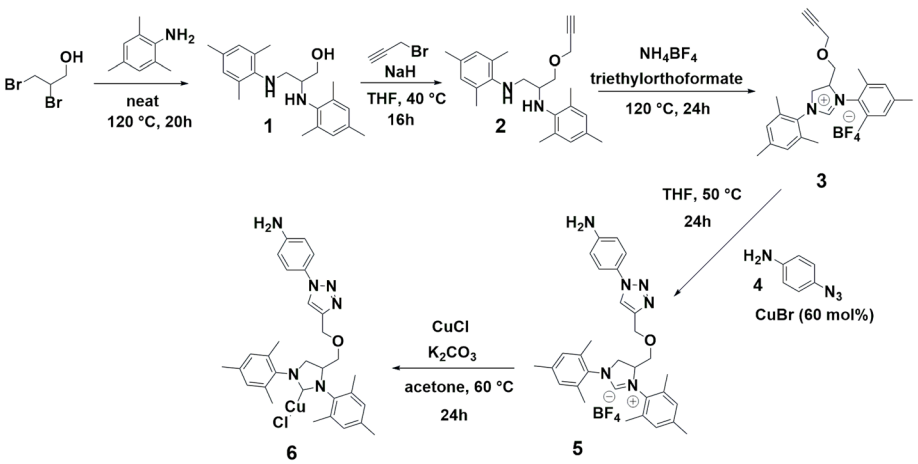

Scheme 1 Synthesis of aniline functionalized NHC–Cu(I) complex **6**.

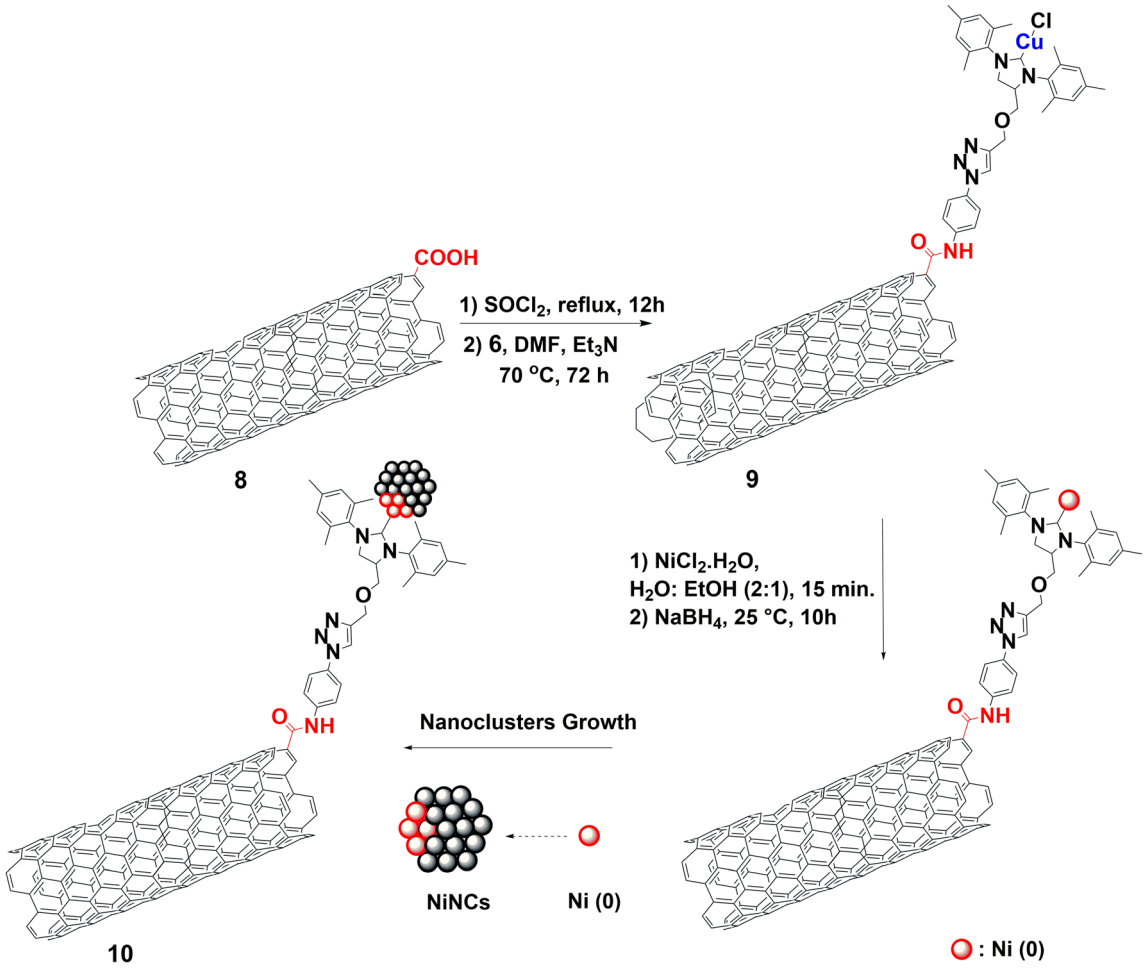

Scheme 2 Preparation of electrocatalyst **10**.

scan revealing characteristic peaks for C 1s, N 1s, O 1s, Cu 2p, and Cl 2p. High-resolution spectra of N 1s, C 1s, and Cu 2p validate the successful integration of complex **6** on oMWCNTs, highlighting the presence of triazole,[41] and NHC moieties along with the Cu(I) oxidation state in **9** (Fig. S26‡).[42]

Following NHC-ligation with NiNCs in electrocatalyst **10**, the I_D/I_G ratio as well as the G and D band positions remain stable, indicating a minimal impact on the MWCNT surface and the persistence of NHC–metal ligation, respectively (Fig. S27–S28 and Table S1‡). A 13 cm^{-1} downshift in the C=O stretching frequency found at 1702 cm^{-1} in the ATR-FTIR spectrum suggests an interaction between the carbonyl groups of **8** and NiNCs, supporting the NHC–NiNC ligation on oMWCNTs (**8**) (Fig. S29–S30‡).

The XPS survey scan spectra confirm the engineered nanostructure of **10** (Fig. S31‡) detecting all relevant elements: C 1s, N 1s, O 1s and Ni 2p. Importantly, the absence of Cu 2p signals validates the efficiency of the transmetalation method in generating NHC–NiNCs (Fig. S31‡). Additionally, the atomic percentage of Ni/C, determined from the normalized areas of Ni and C peaks, is calculated to be only 3.9%. High-resolution N 1s spectra revealed three distinct components at binding energies (BE) of 399.2 eV, 400.2 eV and 401.8 eV (Fig. 1a and Table S2‡) in a 1 : 3:1 ratio. The lowest BE at 399.2 eV is attributed to the N–C–Ni(0) atom of the N-heterocyclic carbene, appearing at 1.0 eV lower than the analogous N–C–Cu(I) in **9**.[42] This shift reflects the electron-richer carbene ligand species bonded to Ni(0) atoms in the NiNCs. Narrow C 1s scans further corroborate the successful preparation, with characteristic components fitted and assigned (Fig. 1b and Table S2‡). Notably, the normalized areas show a 1 : 1 ratio between the N–C–Ni at 282.8 eV,[43] and the MWCNTs-COONH- component at 289.1 eV, directly aligning with electrocatalyst **10**'s rational design. Ni 2p spectra (Fig. 1c) revealed a distinct component, at 852.7 eV, confirming the presence of Ni (0), alongside the predominant component at 856.8 eV, attributed to oxidized Ni^{n+}.[44] Although this binding energy falls within the reported range of both Ni(II) and Ni(III), the observed shake-up satellites strongly support the assignment to Ni(II).[45] The selective stabilization of Ni(0) by NHC ligands highlights their strong metal-binding affinity and electronic tuning properties, which confer electronic conductivity and structural integrity to electrocatalyst **10**.[21–23] The predominance of oxidized Ni^{n+} is consistent with the very reactive Ni(0) nano species due to the very small size and clean surface state rendering Ni(0) highly prone to oxidation under atmospheric and aqueous conditions.[46] This dual functionality—where the

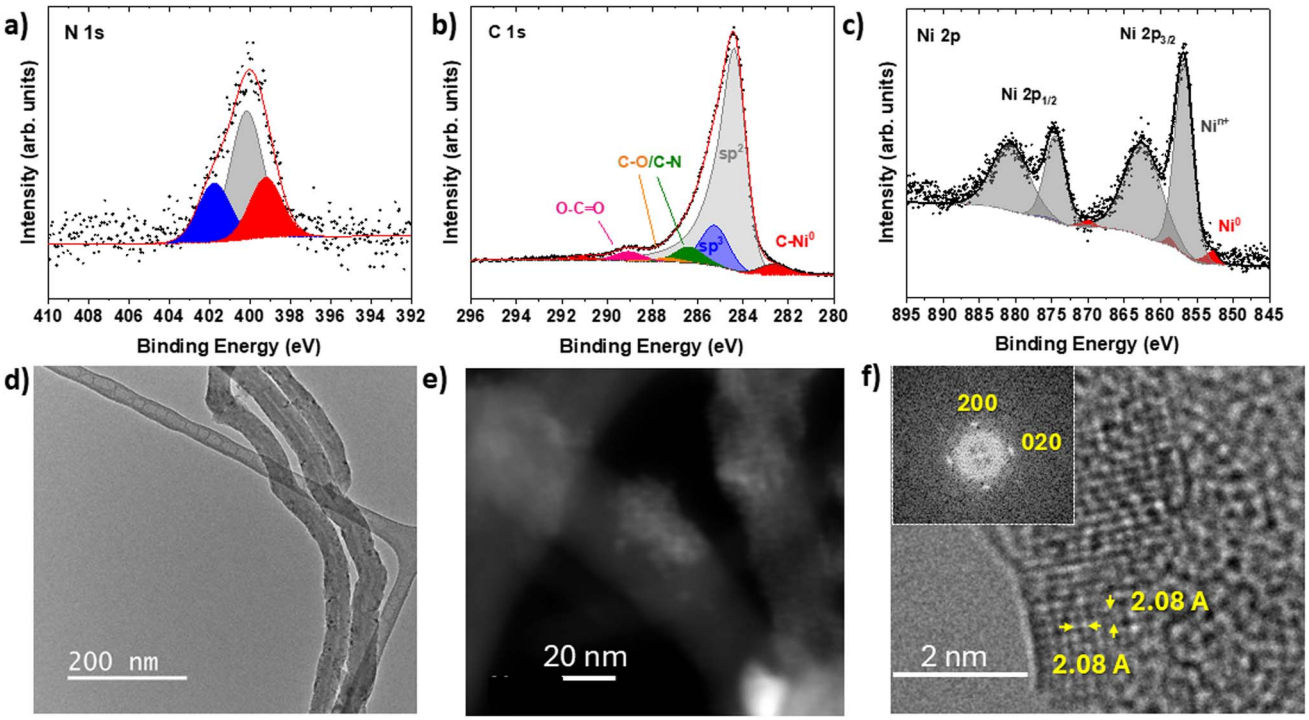

Fig. 1 (a) XPS narrow scans of N 1s, (b) C 1s, (c) Ni 2p and (d) TEM image of **10**, (e) HAADF-STEM image of **10** and (f) HRTEM-atomic resolved image of NiNCs of **10** with the corresponding lattice fringes (inset: FFT).

NHC-stabilized Ni(0) core ensures stability and provides a conductive support, while the oxidized NiO_x shell acts as the electroactive surface for the OER—underscores the synergistic balance achieved in the engineered nanostructure of electrocatalyst **10**.

Low magnification TEM images show the presence of MWCNTs (Fig. 1 d). The High-Resolution Transmission Electron Microscopy (HRTEM) study allows identifying the presence of crystalline nanoclusters on the surface of MWCNTs as well as graphitic and amorphous particles containing small crystalline nanoclusters in agglomerates surrounding MWCNTs' surface. The Energy-Dispersive X-ray Spectroscopy (EDS) analysis indicates the presence of Ni in both the MWCNT surface and the surface's surrounding agglomerates. Moreover, a Scanning Transmission Electron Microscopy (STEM) study has been performed. The high-angle annular dark-field scanning transmission electron microscopy (HAADF-STEM) images reflect the presence of more intense areas both in the surface and surrounding agglomerates suggesting—according to the higher atomic number of Ni against C—the presence of Ni (Fig. 1e, S32 and S33‡). This is confirmed with the simultaneous acquisition of EDS spectra in each scanning position (Fig. S32 and S33‡). EDS maps confirm the presence of Ni in the brighter areas and the existence of NiNCs. The interatomic distances of 2.08 Å measured in the NiNCs and the corresponding FFTs (Fig. 1f) are compatible with the fcc NiO unit cell along the [001] zone axis. The identification of NiO lattice fringes, a well-known Ni(II) phase, provides additional structural confirmation that the oxidized species observed by XPS corresponds to Ni(II) rather than Ni(III). The ensemble of these structural and compositional data allows validating the efficient decoration of NiNCs on MWCNTs. Given the exceptionally small size (<1.6 nm) and high surface area of the NiNCs, the oxidation easily occurs on the surface shell, while the NHC ligation stabilizes effectively the Ni(0) core, in accordance with the XPS findings.[47–49]

The electrocatalytic performance of electrocatalyst **10** was evaluated for the OER in aqueous 0.1 M KOH electrolyte solution at room temperature and compared against oMWCNTs **8**, its MWCNTs-Cu(I)NHC precursor **9**, and the benchmark $\mathbf{RuO_2}$. Linear sweep voltammetry (LSV) polarization curves were recorded within the potential range of 0.8–2.0 V *vs.* RHE, with iR compensation applied and normalized to the geometric electrode surface area (A = 0.196 cm^2). Upon immersion of electrode **10** into 0.1 M KOH electrolyte, surface hydration of Ni(II) species to $Ni(OH)_2$ occurs spontaneously on the NiNC surface, consistent with previous reports.[49] During operation, the NiNCs in **10** undergo surface oxidation, leading to the formation of highly electroactive NiOOH species, as evidenced by the oxidation peak associated with the Ni(II)/Ni(III) transition ($Ni(OH)_2$/NiOOH conversion), occurring just prior to the OER onset (Fig. 2a).[50] Over the course of 1000 CV cycles, **10** undergoes progressive surface restructuring, with the Ni(II)/Ni(III) oxidation peak at 1.43 mV—with a full width half maximum (FWHM = 0.079), characteristic of highly uniform redox active species in nanoclusters—shifting to an even narrower peak at 1.39 mV (Fig. 2a) with a further 8% decrease in FWHM (Fig. S34‡). This shift reflects stabilization into a dynamic equilibrium between $Ni(OH)_2$ and NiOOH, eventually resulting in a stable Ni(II)/Ni(III) oxidation potential.[51,52]

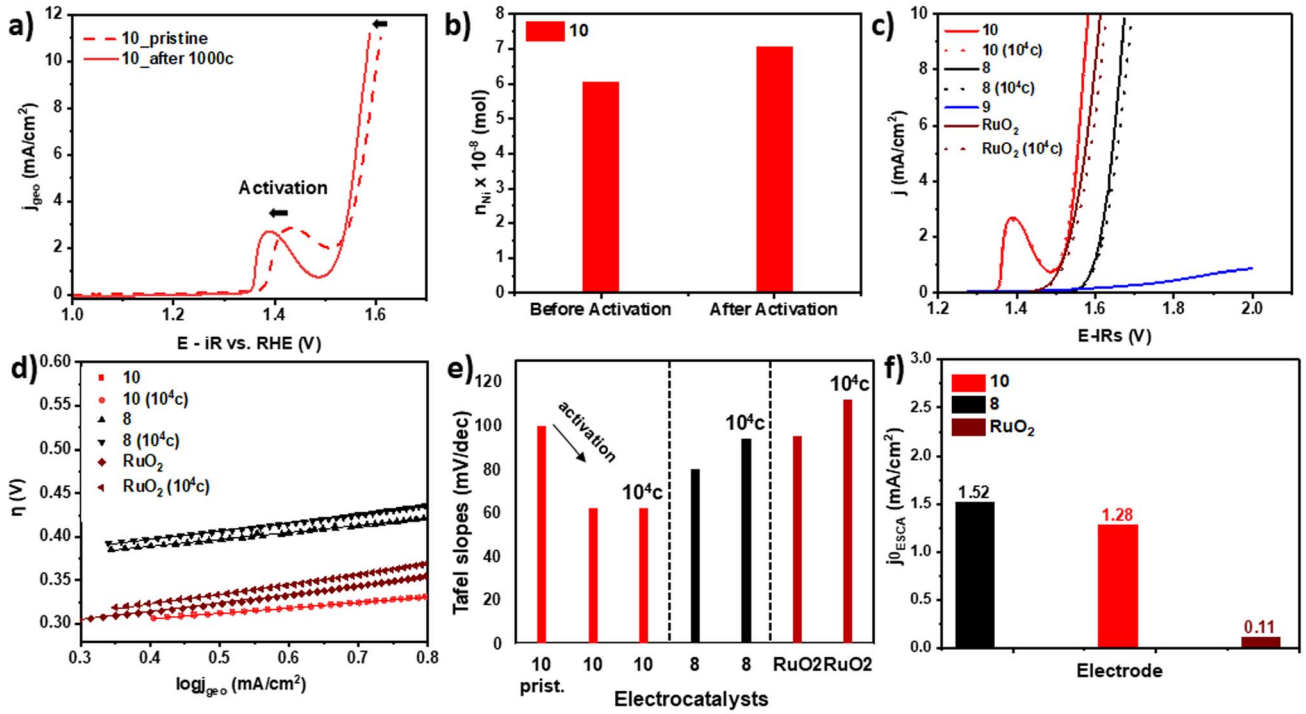

Fig. 2 (a) LSV polarization curves obtained at 1600 rpm rotation speed and 5 mV s^{-1} scan rate in 0.1 M KOH for pristine **10** and **10** after activation, (b) tabulated n_{Ni} (mol) of **10** before (pristine **10**) and after activation, (c) LSV polarization curves obtained at 1600 rpm rotation speed and 5 mV s^{-1} scan rate in 0.1 M KOH of **10**, **9**, **8** and **RuO_2** before and after 10^4 successive LSV cycles, (d) Tafel slopes of **10**, **8** and **RuO_2** before and after 10^4 successive LSV cycles, (e) tabulated comparative Tafel values of **10** (pristine **10**, **10** and **10** after 10^4 cycles), **8** (**8** and **8** after 10^4 cycles) and **RuO_2** (**RuO_2** and **RuO_2** after 10^4 cycles) and (f) tabulated comparative $j0_{ECSA}$ values of **10**, **8** and **RuO_2**.

Linear sweep voltammetry (LSV) measurements recorded before and after electrode activation revealed that electrode **10** exhibited an overpotential of 370 mV (η_{10}) to achieve a current density of 10 mA cm^{-2}, which decreased to 350 mV following activation (Fig. 2a). Furthermore, at a higher current density of 80 mA cm^{-2}, the electrode displayed an overpotential of 670 mV (Fig. S35‡), positioning **10** among the highly efficient electrocatalysts for the OER.[5] To quantify the electroactive Ni sites (n_{Ni}, mol) available on electrode **10** and evaluate the impact of the activation process on surface restructuring and performance stabilization, the electroactive Ni surface species (n_{Ni}) participating in the OER catalytic process were determined both before and after activation (Fig. S34‡).[53] By integrating the anodic oxidation peak prior to the OER onset, the electroactive Ni was calculated to be 6.05×10^{-8} mol before activation. Following the activation process, the electroactive Ni content increased significantly to 7.05×10^{-8} mol, representing a 16.5% enhancement in the available active sites in the optimized surface structure (Fig. 2b). Indeed, electrocatalyst **10** outperforms the highly efficient electrocatalyst **8** by 100 mV and slightly exceeds the benchmark electrocatalyst **RuO_2** by 30 mV (Table 1). Concretely, **8** exhibits efficient electrocatalytic activity with an overpotential η_{10} of 450 mV consistent with prior reports.[24] However, after functionalization with the Cu(I)–carbene complex **6**, nanomaterial **9** completely loses its electroactivity towards the OER. In contrast, the incorporation of NHC-ligated NiNCs in **10** not only restored but further enhanced its electrocatalytic activity by 100 mV (Fig. 2c). This stark difference in OER performance highlights the role of the metal center and surface functionality. In nanomaterial **8**, surface –COOH groups facilitate proton-coupled electron transfer (PCET), enabling efficient OER activity. However, in **9**, these are replaced by

Table 1 Electrochemical data of targeted electrocatalyst **10** and comparison with reference nanomaterials **8**, **9** and **RuO_2**. All potentials are measured at 10 mA cm^{-2} current density. LSVs were measured under identical conditions: 0.1 M KOH, 1.600 rpm rotation speed, 5 mV s^{-1} scan rate and electrode preparation

Material	E_{10} *vs.* RHE*	E_{10} *vs.* RHE (10^4 c)	η_{10}	R_{ct}	Tafel slopes (1c/10^4c)	$j0_{ECSA}$	Specific activity j_{ECSA}
8	1.68 V	1.69 V	450 mV	133 Ω	80/94 mV dec^{-1}	1.52 mA cm_{ECSA}^{-2}	1.5 mA cm_{ECSA}^{-2}
9	—[a]	—[a]	—[a]	6711 Ω	—	—	—
10	1.58 V	1.58 V	350 mV	55 Ω	62/62 mV dec^{-1}	1.28 mA cm_{ECSA}^{-2}	15.3 mA cm_{ECSA}^{-2}
RuO_2	1.62 V	1.63 V	390 mV	114 Ω	95/112 mV dec^{-1}	0.11 mA cm_{ECSA}^{-2}	0.6 mA cm_{ECSA}^{-2}

[a] Nanomaterial presents no electroactivity and does not reach a current density of 10 mA cm^{-2}.

electronically inert –CONH linkages, while NHC–Cu(I) complexes further passivate the surface. Cu(I), with its d^{10} closed-shell configuration, remains redox-inactive under OER conditions and does not form catalytically active oxyhydroxide species. In contrast, nanomaterial **10** contains NHC–Ni(0)NiO_x nanoclusters that dynamically restructure under increasing anodic potentials to form high-valent Ni oxyhydroxide phases, well-known as OER-active phases. These differences explain why **10** outperforms greatly both **8** and **9** in the OER. Notably, consistent performance was observed across five independent synthetic batches of electrocatalyst **10**, confirming both its synthetic reproducibility and operational robustness in the OER (Table S3‡).

The stability of electrocatalyst **10** was then evaluated over 10^4 cycles and compared to the previously demonstrated efficient electrocatalysts **8** and **RuO_2** (Fig. 2c and Table 1). Electrocatalyst **10** maintains its electrocatalytic performance with no measurable η_{10} gain, while **8** and **RuO_2** show only minor gains of 10 mV (Fig. 2c, dotted lines). In addition, the retention of active nickel sites after 10^4 OER cycles—as calculated with only a slight 0.46% decrease—highlights the excellent electroactive surface stability and sustained OER activity of **10** promoted by the effective ligation of MWCNTs–NHC–Ni(0) (Fig. S36‡). Long-term potentiometry for over 5 hours at 10 mA cm^{-2} was also conducted, showing a minimal gain of 15 mV in overpotential, corresponding only to a 0.94% increase (Fig. S37‡).

Tafel slopes were determined for **8**, **10**, and **RuO_2** in the low-potential region immediately after the interference from the Ni(II)/Ni(III) oxidation peak of **10** to ensure accuracy (Fig. 2d and Table 1). Electrocatalyst **10** demonstrates the lowest Tafel slope of 62 mV dec^{-1}, outperforming **8** and **RuO_2**, which exhibit slopes of 80 mV dec^{-1} and 95 mV dec^{-1}, respectively, indicating significantly faster OER kinetics for **10**. Notably, after 10^4 OER cycles, the Tafel slopes of **8** and **RuO_2** increase by 17.5% and 17.9%, respectively, indicating a decline in kinetic efficiency over prolonged cycling. In contrast, electrocatalyst **10** maintains its initial Tafel slope, showcasing superior kinetic stability under extended operational conditions (Fig. 2d and e). To gain deeper mechanistic insights into electrocatalyst **10**,[54] Tafel slopes were compared before and after activation (Fig. 2e and S38‡). Initially, pristine **10** exhibited a Tafel slope of 97 mV dec^{-1}, indicating a more kinetically hindered surface-controlled process, with a rate-determining step (RDS) involving surface restructuring and the initial oxidation of Ni(II) to active NiOOH species. After activation, the Tafel slope decreased significantly to 62 mV dec^{-1}, reflecting a diffusion-assisted regime, where OH^- ion adsorption and PCET steps dominate, with an RDS likely involving PCET on stabilized NiOOH sites.[55,56] Finally, the unchanged slope after prolonged cycling further indicates the robustness of the activated surface and the minimized impact of mass transport limitations.

The exchange current density ($j0$) provides key insight into the intrinsic efficiency of electron transfer at the electrode/electrolyte interface, reflecting the inherent activity of electrocatalysts.[57] It was obtained by Tafel extrapolation and was normalized by the geometric electrode surface area. Before activation, electrocatalyst **10** exhibits a high $j0$ of 1.87 mA cm^{-2}, which improves to 1.91 mA cm^{-2} after activation and remains stable even after 10^4 OER cycles, underscoring its exceptional kinetic robustness (page S36‡). Electrocatalyst **8** demonstrates a slightly higher $j0$ of 2.27 mA cm^{-2}, while **RuO_2** shows a slightly lower value of 1.89 mA cm^{-2}. Despite the inherently high $j0$ of **10**, we further analyzed its intrinsic activity by normalizing $j0$ to the electrochemically active surface area (ECSA) for a fair comparison across materials with differing characteristics. The ECSA of **8**, **9**, **10** and **RuO_2** was calculated from double-layer capacitance (C_{dl}) measurements in non-faradaic regions of CVs at different scan rates (Fig. S39–S42 and Table S4‡).[58,59] When normalized by ECSA, the $j0_{ECSA}$ of **10** is 1.28 mA cm_{ECSA}^{-2}, only 0.24 mA cm^{-2} lower than that of **8** but surpassing the benchmark **RuO_2** by an impressive 12-fold (Fig. 2f and Table 1), highlighting the very efficient intrinsic kinetic activity of electrocatalyst **10**.

To delve further into the performance of electrocatalyst **10**, the specific activity per unit surface area (j_{ECSA}) and intrinsic activity per Ni electroactive site ($j_{n\mathrm{Ni}}$) were evaluated across various overpotentials. Electrocatalyst **10** exhibits a remarkable specific activity, starting at 1.3 mA cm_{ECSA}^{-2} at an overpotential of 300 mV and reaching 15.3 mA cm_{ECSA}^{-2} at 380 mV, significantly outperforming both **8** (10-fold) and **RuO_2** (25-fold) (Fig. 3a and Table 1 and S43‡). This exceptional enhancement highlights the efficient utilization of electroactive Ni sites in **10**, attributed to its rationally engineered nanostructure, which enables a high catalytic turnover per unit surface area. Furthermore, electrocatalyst **10** demonstrates an outstanding intrinsic activity (Fig. S44‡),[60] increasing from 2.83×10^7 mA $mol^{-1} \cdot cm^{-2}$ at 300 mV to 1.65×10^8 mA $mol^{-1} \cdot cm^{-2}$ at 360 mV (Fig. 3b). This significant increase reflects the enhanced accessibility and reactivity of the Ni^{III} active centers within the nanostructure of **10**, facilitated by the synergistic interplay between the MWCNT-supported NHC-stabilized Ni(0) core providing a conductive support to the electroactive oxidized Ni^{n+} shell species. This unique nanoarchitecture facilitates fast electron transfer kinetics and maximizes the utilization of every electroactive Ni site, positioning **10** as a highly efficient and intrinsically active OER electrocatalyst, significantly outperforming benchmark catalysts.[61]

The turnover frequency (TOF), a critical parameter reflecting the catalytic activity per active site, was also calculated for electrocatalyst **10** across various overpotentials (Fig. 3c).[52,62] At 360 mV, corresponding to j_{geo}@10 mA cm^{-2}, electrocatalyst **10** demonstrates a very high TOF of 0.46 s^{-1} per mole of Ni, underscoring the high activity and accessibility of its electroactive Ni sites (page S42‡) and highlighting the efficiency of its rationally engineered nanostructure. Furthermore, the linearity of the log TOF *vs.* η plot (Fig. 3d) and its slope of 62 mV dec^{-1} further validate the OER kinetics of **10**, consistent with the Tafel slope, underlining the efficient, uniform activation of the electroactive Ni sites, further supporting PCET as the RDS.

Electrochemical impedance spectroscopy (EIS) was employed to investigate the charge transfer kinetics and capacitive properties of electrocatalyst **10**,[63] benchmark **RuO_2**, and comparative starting materials **8** and **9** (Fig. 3e). The Nyquist plots modeled with a Randles circuit containing

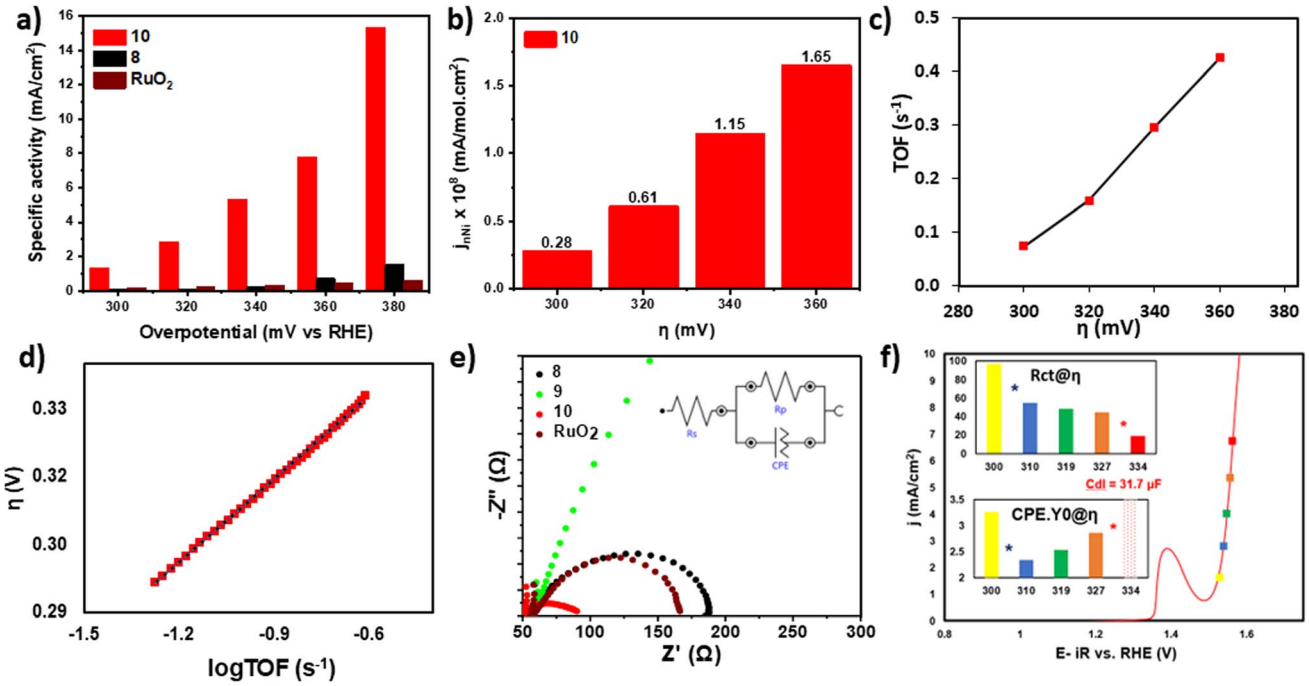

Fig. 3 (a) Tabulated values of specific activity j_{ECSA} of **10**, **8** and **RuO$_2$** across various overpotentials, (b) tabulated values of the intrinsic activity j_{nNi} of **10** across various overpotentials, (c) TOF as a function of η for electrocatalyst **10**, (d) logarithmic TOF (log TOF) as a function of η for electrocatalyst **10**, (e) Nyquist plots of **10**, **9**, **8** and **RuO$_2$** (inset: applied Randles circuit fit) and (f) R_{ct} and CPE.Y0 across various overpotentials for **10**. RDS changes are marked with stars.

a constant-phase element (CPE) reveal significant differences in charge transfer resistances (R_{ct}) among the samples (Table S5‡). Electrocatalyst **8** exhibits a moderate R_{ct} of 133 Ω, while upon functionalization with the NHC–Cu(I) complex in **9**, R_{ct} skyrockets to thousands of Ω, underscoring the detrimental impact of this intermediate on charge transport. However, the formation of NHC–NiNCs in electrocatalyst **10** restores and dramatically enhances charge transfer efficiency, resulting in an R_{ct} value 2.5 times lower than that of **8** and nearly half that of **RuO$_2$**. The overall decrease in R_{ct} reflects improved charge transport and enhanced electrical conductivity in **10**.[64] Additionally, Fig. 3f insets illustrate the detailed evaluation of R_{ct} and capacitive properties at 0.1 M KOH, at various η. The bar chart (top inset, Fig. 3f) confirms a progressive decrease in R_{ct} with increasing overpotential for electrocatalyst **10**, demonstrating efficient electron transfer during the OER process. The relationship between η and R_{ct} was analyzed across the kinetic region of the OER, corresponding to current densities up to 7 mA cm^{-2} (Fig. S45‡). Two distinct transitions are observed in the Nyquist-derived R_{ct} values: a sharp decrease at approximately 2.5 mA cm^{-2} and an even steeper drop at 7 mA cm^{-2}. These transitions likely correspond to changes in the RDS of the OER mechanism.[59] At lower current densities, the initial R_{ct} decrease suggests the onset of faster PCET kinetics, possibly associated with Ni(II)/Ni(III) oxidation. The second, more pronounced decline in R_{ct} at 7 mA cm^{-2} likely reflects the transition to the oxygen evolution step, where surface oxygen species become the dominant intermediates. These observations underscore the dynamic restructuring of the electroactive surface of electrocatalyst **10**, highlighting its adaptive behavior in achieving efficient charge transfer across different kinetic regimes of the OER process.[13,65]

After the comprehensive electrochemical evaluation in 0.1 M KOH, the study of **10** was extended to approach conditions closer to practical applications. The LSV polarization curve of **10** was recorded up to 200 mA cm^{-2} in the more concentrated alkaline environment, 1 M KOH (Fig. 4a), giving outstanding overpotentials η_{10} of 320 mV, η_{100} of 420 mV, and η_{200} of 500 mV. The improved ionic conductivity in 1 M KOH likely mitigates diffusion-limiting factors, enhancing charge transport and ensuring more efficient catalytic activity at higher current densities.[66,67] This is also reflected by the smaller Tafel slope of 51 mV dec^{-1}, suggesting that in 1 M KOH, the RDS involves the oxidation of adsorbed hydroxide species (OH*) to oxygen intermediates (O*), a step commonly associated with high-performance OER catalysts (Fig. 4b).[68] The $j0$ and $j0_{ECSA}$ values are 1.86 mA cm^{-2} and 1.24 mA cm^{-2}, respectively, whereas the j_{ECSA} at η_{350} is 17 mA cm$_{ECSA}{}^{-2}$ reaching 133 mA cm$_{ECSA}{}^{-2}$ at η_{500} (Fig. 4c and S46‡) and the intrinsic activity j_{nNi} at η_{350} is 3.6 $\times$ 10^8 mA mol^{-1} cm^2 with a $j_{nNi} = 2.8 \times 10^9$ mA mol^{-1} cm^2 at η_{500} (Fig. 4d and S47‡).

The TOF values further reinforce these metrics, with **10** achieving a TOF of 7.4 s^{-1} at 500 mV (Fig. 4e). This substantial metric emphasizes how the increased hydroxide ion availability and improved charge transport in 1 M KOH enables significantly faster reaction kinetics and higher TOF values. Furthermore, catalyst **10** demonstrates highly rapid charge transfer kinetics at higher η, with a significant decrease in R_{ct} from 66 Ω

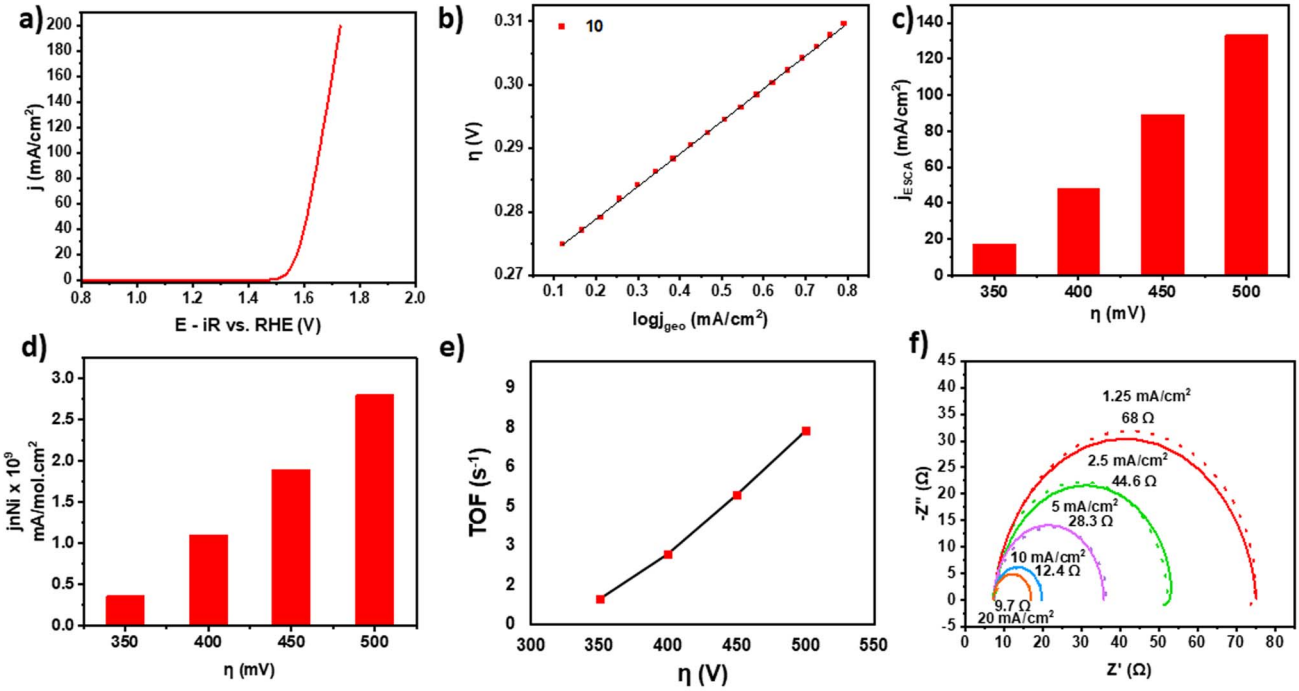

Fig. 4 (a) LSV polarization curve obtained at 1600 rpm rotation speed and 5 mV s^{-1} scan rate in 1 M KOH for **10** reaching up to 200 mA cm^{-2}, (b) Tafel slope of **10** in 1 M KOH, (c) tabulated values of the specific activity of **10** across various overpotentials in 1 M KOH, (d) tabulated values of the intrinsic activity of **10** across various overpotentials in 1 M KOH, (e) TOF plot of **10** across 350–500 mV overpotentials in 1 M KOH and (f) Nyquist plots of **10** (dots) with applied Randles circuit fit (lines) obtained at various *j* (mA cm^{-2}) in 1 M KOH.

at $\eta_{1.25}$ to 9.7 Ω at η_{20} (Table S6‡). The C_{dl} decreases consistently from 51.0 μF to 35.6 μF, due to increased surface coverage by reaction intermediates (OH*, O*) and thinning of the double layer, reflecting efficient interfacial processes. The substantially smaller solution resistance (R_s) in 1 M KOH (~7.5 Ω) confirms the elimination of diffusion limitations, under these conditions. The Tafel slope derived from $\log(1/R_{ct})$, 54 mV dec^{-1} (Fig. S48‡), aligns closely with the polarization-derived Tafel slope, 51 mV dec^{-1}, pointing to similar kinetic behavior, in which surface-controlled charge transfer processes dominate without significant contributions from diffusion complexities. Such alignment strengthens the hypothesis that the RDS involves the formation or oxidation of adsorbed intermediates (OH* or O*).

Finally, the durability was evaluated in 1 M KOH, at 10 mA cm^{-2} for ~3 hours, demonstrating a minimal gain of 20 mV in overpotential, corresponding to only a 1.3% increase (Fig. S49‡). Interestingly, we recorded a post-test LSV (Fig. S50‡), which showed the near disappearance of the characteristic Ni(II)/Ni(III) redox peak, with only a faint shoulder visible at higher potentials and partially merged with the OER onset. This suggests progressive oxidation of surface Ni species into higher-valent Ni^{3+}/Ni^{4+} states within the NiO_x shell under prolonged anodic polarization. This phenomenon is consistent with prior studies, where extended electrochemical operation induced phase transitions and suppression of redox features due to the stabilization of higher oxidation states and restructuring of the active surface, while preserving electrocatalytic activity.[69] Importantly, in electrocatalyst **10**, this transformation correlates with only a minor performance loss (14 mV gain at 10 mA cm^{-2}), confirming the robustness and adaptability of the NiO_x catalytic surface during extended operation. Additionally, after 10^4 cycles in 1 M KOH, **10** maintained its performance with only a 15 mV overpotential gain and negligible change in Ni active sites (<0.1%), further confirming its durability (Fig. S51‡).

Conclusion

In conclusion, NHC-ligated NiNCs anchored covalently on MWCNTs were prepared *via* a dual metal-reduction and transmetalation strategy, creating a precisely engineered robust nanoarchitecture. Leveraging the unique tuning properties of NHC–M(0) ligation, the NHC–Ni(0) core provides exceptional stabilization and conductivity, supporting the formation of an electroactive NiO_x shell, as confirmed by XPS and HRTEM studies. This synergistic design achieves efficient mechanistic progression through all OER steps. In 0.1 M KOH, the catalyst exhibits a low overpotential of 350 mV at 10 mA cm^{-2}, with activation enhancing performance through the dynamic formation of a stabilized NiOOH shell. The catalyst outperforms the RuO_2 benchmark in overpotential, *j*0, Tafel slopes, charge transfer resistance and specific activity, highlighting the efficient utilization of electroactive Ni sites. Under industrially relevant conditions (1 M KOH, 200 mA cm^{-2}), electrocatalyst **10** achieves very low overpotentials ($\eta_{10} = 320$ mV, $\eta_{200} = 500$ mV), exceptional TOF values up to 7.4 s^{-1}, and remarkable specific ($j_{ECSA} = 133$ mA cm^{-2}) and intrinsic ($j_{nNi} = 2.8 \times 10^9$ mA mol^{-1}

cm^2) activities, effectively overcoming diffusion limitations observed in less concentrated electrolytes. EIS analysis revealed highly efficient charge transfer kinetics, with R_{ct} decreasing from 66 Ω to 9.7 Ω and C_{dl} declining consistently due to increased surface coverage by intermediates. The alignment of Tafel slopes derived from polarization (51 mV dec^{-1}) and impedance (54 mV dec^{-1}) confirms a surface-controlled charge transfer mechanism, with the RDS involving intermediate OH*/O* formation or oxidation. Durability tests confirm the catalyst's robustness, with minimal overpotential gains (0.9% and 1.3%) and <0.5% apparent loss of Ni active sites after 10 000 cycles. The ultrafine size (<1.6 nm) and high dispersion of NiNCs expose nearly all electroactive Ni sites in the NiO_x shell, maximizing catalytic efficiency. The NHC–Ni(0) core ensures structural stability and conductivity, while MWCNTs enhance electron transport and provide robust mechanical support, enabling efficient charge transport kinetics and enhanced durability under harsher electrochemical conditions. These findings position NHC-ligated NiNCs on MWCNTs as a scalable, durable, and highly efficient electrocatalyst for sustainable OER applications, surpassing state-of-the-art Ni-based and RuO_2 benchmarks (Table S7‡).

Data availability

All data supporting the findings of this study are included in the manuscript and its ESI.‡ Additionally, the raw datasets are available from the corresponding authors, upon reasonable request.

Author contributions

Rapakousiou Amalia: conceptualization, data curation, formal analysis, funding acquisition, investigation, methodology, project administration, resources, supervision, validation, visualization, writing–original draft, writing–review and editing. Savvas G. Chalkidis: data curation, formal analysis, investigation, validation, writing–review and editing. Michail P. Minadakis: data curation, formal analysis, investigation, validation, writing–review and editing. María Luisa Ruiz-González: HRTEM/EDS/HAADF-STEM: data curation, formal analysis, investigation, resources, validation, writing–review and editing. Cristina Navio: XPS: data curation, formal analysis, investigation, resources, validation, visualization, writing–review and editing. Georgios C. Vougioukalakis: conceptualization, resources, supervision, validation, writing–review and editing. Nikos Tagmatarchis: conceptualization, resources, supervision, validation, writing–review and editing.

Conflicts of interest

There are no conflicts to declare.

Acknowledgements

The research project was supported by the Hellenic Foundation for Research and Innovation (H.F.R.I.) under the "2nd Call for H.F.R.I. Research Projects to support Post-Doctoral Researchers" granted to A.R. (NANOElectroCAT, project Number 913). A. R. acknowledges the support of ELECMI-CNME, Spain, for granting distinguished free access to ELECMI facilities and also thanks Dr A. Kagkoura for useful scientific discussions.

References

1 H. Wang, K. H. L. Zhang, J. P. Hofmann, V. A. de la Peña O'Shea and F. E. Oropeza, *J. Mater. Chem. A*, 2021, **9**, 19465–19488.
2 E. Fabbri and T. J. Schmidt, *ACS Catal.*, 2018, **8**, 9765–9774.
3 S. R. Edea and Z. Luo, *J. Mater. Chem. A*, 2021, **9**, 20131–20163.
4 A. Vazhayil, L. Vazhayal, J. Thomas, S. Ashok C and N. Thomas, *Appl. Surf. Sci. Adv.*, 2021, **6**, 100184.
5 M. Tahir, L. Pan, F. Idrees, X. Zhang, L. Wang, J.-J. Zou and Z. L. Wang, *Nano Energy*, 2017, **37**, 136–157.
6 K. S. Joya, L. Sinatra, L. G. AbdulHalim, C. P. Joshi, M. N. Hedhili, O. M. Bakr and I. Hussain, *Nanoscale*, 2016, **8**, 9695–9703.
7 X. Yan, L. Tian and X. Chen, *J. Power Sources*, 2015, **300**, 336–343.
8 F.-T. Tsai, Y.-T. Deng, C.-W. Pao, J.-L. Chen, J.-F. Lee, K.-T. Lai and W.-F. Liaw, *J. Mater. Chem. A*, 2020, **8**, 9939–9950.
9 S. Funaki, T. Kawawaki, T. Okada, K. Takemae, S. Hossain, Y. Niihori, T. Naito, M. Takagi, T. Shimazaki, S. Kikkawa, S. Yamazoe, M. Tachikawa and Y. Negishi, *Nanoscale*, 2023, **15**, 5201–5208.
10 Y.-C. Zhang, C. Han, J. Gao, L. Pan, J. Wu, X.-D. Zhu and J.-J. Zou, *ACS Catal.*, 2021, **11**, 12485–12509.
11 L. Yang, Q.-X. Du, J. Cui, H.-W. Yang and H. Qian, *Inorg. Chem.*, 2024, **63**, 1954–1961.
12 M. Kim, H. Han, K. Lee, S. Kang, S.-H. Lee, S. H. Lee, H. J, J. H. Ryu, C.-Y. Chung, K. M. Kim and S. Mhin, *J. Mater. Chem. A*, 2024, **12**, 17596–17606.
13 P. Chakthranont, J. Kibsgaard, A. Gallo, J. Park, M. Mitani, D. Sokaras, T. Kroll, R. Sinclair, M. B. Mogensen and T. F. Jaramillo, *ACS Catal.*, 2017, **7**, 5399–5409.
14 M. González-Ingelmo, M. López García, F. E. Oropeza, P. Álvarez, C. Blanco, R. Santamaría and V. G. Rocha, *J. Mater. Chem. A*, 2023, **11**, 24248–24260.
15 H. Lei, Z. Wang, F. Yang, X. Huang, J. Liu, Y. Liang, J. Xie, M. S. Javed, X. Lu, S. Tan and W. Mai, *Nano Energy*, 2020, **68**, 104293.
16 D. M. Morales, M. A. Kazakova, S. Dieckhöfer, A. G. Selyutin, G. V. Golubtsov, W. Schuhmann and J. Masa, *Adv. Funct. Mater.*, 2020, **30**, 1–12.
17 G. Chen, H. Xiang, Y. Guo, J. Huang, W. Chen, Z. Chen, T. Li and K. K. Ostrikov, *Carbon Energy*, 2024, **6**, e522.
18 H. Shen, G. Tian, Z. Xu, L. Wang, Q. Wu, Y. Zhang, B. K. Teo and N. Zheng, *Coord. Chem. Rev.*, 2022, **458**, 214425.
19 M. Ghosh and S. Khan, *ACS Catal.*, 2023, **13**, 9313–9325.
20 A. Rapakousiou, M. P. Minadakis, S. G. Chalkidis, M. L. Ruiz-González, C. Navio, G. C. Vougioukalakis and

N. Tagmatarchis, *ACS Appl. Mater. Interfaces*, 2025, **17**(19), 28138–28150.
21 P. Bellotti, M. Koy, M. N. Hopkinson and F. Glorius, *Nat. Rev. Chem*, 2021, **5**, 711–725.
22 J.-F. Soulé, H. Miyamura and S. Kobayashi, *J. Am. Chem. Soc.*, 2013, **135**, 10602–10605.
23 D. Bouzouita, J. M. Asensio, V. Pfeifer, A. Palazzolo, P. Lecante, G. Pieters, S. Feuillastre, S. Tricard and B. Chaudret, *Nanoscale*, 2020, **12**, 15736–15742.
24 X. Lu, W.-L. Yim, B. H. R. Suryanto and C. Zhao, *J. Am. Chem. Soc.*, 2015, **137**, 2901–2907.
25 G. C. Vougioukalakis and R. H. Grubbs, *Chem. Rev.*, 2010, **110**, 1746–1787.
26 S. G. Chalkidis and G. C. Vougioukalakis, *Eur. J. Org. Chem.*, 2023, **26**, e202301095.
27 N. V. Tzouras, L. P. Zorba, E. Kaplanai, N. Tsoureas, D. J. Nelson, S. P. Nolan and G. C. Vougioukalakis, *ACS Catal.*, 2023, **13**, 8845–8860.
28 C. Deraedt, M. D'Halluin, S. Lesturgez, L. Salmon, G. Goglio, J. Ruiz and D. Astruc, *Eur. J. Inorg. Chem.*, 2015, **2015**, 1345–1350.
29 O. Santoro, A. Collado, A. M. Z. Slawin, S. P. Nolan and C. S. J. Cazin, *Chem. Commun.*, 2013, **49**, 10483.
30 J.-M. Yuan, X.-H. Chen, X.-H. Chen, Z.-F. Fan, X.-G. Yang and Z.-H. Chen, *Carbon*, 2008, **46**, 1266–1269.
31 V. Datsyuk, M. Kalyva, K. Papagelis, J. Parthenios, D. Tasis, A. Siokou, I. Kallitsis and C. Galiotis, *Carbon*, 2008, **46**, 833–840.
32 D. Astruc, L. Liang, A. Rapakousiou and J. Ruiz, *Acc. Chem. Res.*, 2012, **45**, 630–640.
33 T. Bala, B. L. V. Prasad, M. Sastry, M. U. Kahaly and U. V. Waghmare, *J. Phys. Chem. A*, 2007, **111**, 6183–6190.
34 L. Bokobza and J. Zhang, *Express Polym. Lett.*, 2012, **6**, 601–608.
35 A. Yoshida, Y. Kaburagi and Y. Hishiyama, *Carbon*, 2006, **44**, 2333–2335.
36 S. L. H. Rebelo, A. Guedes, M. E. Szefczyk, A. M. Pereira, J. P. Araújo and C. Freire, *Phys. Chem. Chem. Phys.*, 2016, **18**, 12784–12796.
37 S. Osswald, E. Flahaut, H. Ye and Y. Gogotsi, *Chem. Phys. Lett.*, 2005, **402**, 422–427.
38 D. D. Chronopoulos, C. G. Kokotos, N. Karousis, G. Kokotos and N. Tagmatarchis, *Nanoscale*, 2015, **7**, 2750–2757.
39 Z. Li, L. Deng, I. A. Kinloch and R. J. Young, *Prog. Mater. Sci.*, 2023, **135**, 101089.
40 A. Das, S. Pisana, B. Chakraborty, S. Piscanec, S. K. Saha, U. V. Waghmare, K. S. Novoselov, H. R. Krishnamurthy, A. K. Geim, A. C. Ferrari and A. K. Sood, *Nat. Nanotechnol.*, 2008, **3**, 210–215.
41 A. Rapakousiou, R. Sakamoto, R. Shiotsuki, R. Matsuoka, U. Nakajima, T. Pal, R. Shimada, A. Hossain, H. Masunaga, S. Horike, Y. Kitagawa, S. Sasaki, K. Kato, T. Ozawa, D. Astruc and H. Nishihara, *Chem.–Eur. J.*, 2017, **23**, 8443–8449.
42 R. Richstein, C. Eisen, L. Ge, M. Chalermnon, F. Mayer, B. K. Keppler, J. M. Chin and M. R. Reithofer, *Chem. Commun.*, 2023, **59**, 9738–9741.
43 L. Sha, P. Gao, T. Wu and Y. Chen, *ACS Appl. Mater. Interfaces*, 2017, **9**, 40412–40419.
44 L. Zhi, W. Zhang, L. Dang, J. Sun, F. Shi, H. Xu, Z. Liu and Z. Lei, *J. Power Sources*, 2018, **387**, 108–116.
45 A. P. Grosvenor, M. C. Biesinger, R. St. C. Smart and N. S. McIntyre, *Surf. Sci.*, 2006, **600**, 1771–1779.
46 M. D. de los Bernardos, S. Pérez-Rodríguez, A. Gual, C. Claver and C. Godard, *Chem. Commun.*, 2017, **53**, 7894–7897.
47 W. Su, F. Wu, L. Fang, J. Hu, L. Liu, T. Guan, X. Long, H. Luo and M. Zhou, *J. Alloys Compd.*, 2019, **799**, 15–25.
48 T. Yu, Y. Hou, P. Shi, Y. Yang, M. Chen, W. Zhou, Z. Jiang, X. Luo, H. Zhou and C. Yuan, *Inorg. Chem.*, 2022, **61**, 2360–2367.
49 B. Kim, A. Oh, M. K. Kabiraz, Y. Hong, J. Joo, H. Baik, S.-I. Choi and K. Lee, *ACS Appl. Mater. Interfaces*, 2018, **10**, 10115–10122.
50 H. Ding, H. Liu, W. Chu, C. Wu and Y. Xie, *Chem. Rev.*, 2021, **121**, 13174–13212.
51 N. Hales, T. J. Schmidt and E. Fabbri, *Curr. Opin. Electrochem.*, 2023, **38**, 101231.
52 S. Xie, Y. Yan, S. Lai, J. He, Z. Liu, B. Gao, M. Javanbakht, X. Peng and P. K. Chu, *Appl. Surf. Sci.*, 2022, **605**, 154743.
53 M. Görlin, P. Chernev, J. Ferreira de Araújo, T. Reier, S. Dresp, B. Paul, R. Krähnert, H. Dau and P. Strasser, *J. Am. Chem. Soc.*, 2016, **138**, 5603–5614.
54 L. Negahdar, F. Zeng, S. Palkovits, C. Broicher and R. Palkovits, *ChemElectroChem*, 2019, **6**, 5588–5595.
55 G. Li, L. Anderson, Y. Chen, M. Pan and P.-Y. Abel Chuang, *Sustain. Energy Fuels*, 2018, **2**, 237–251.
56 Y. Matsumoto and E. Sato, *Mater. Chem. Phys.*, 1986, **14**, 397–426.
57 Q. Zhou, L. Liao, H. Zhou, D. Li, D. Tang and F. Yu, *Mater. Today Phys.*, 2022, **26**, 100727.
58 C. Wei, S. Sun, D. Mandler, X. Wang, S. Z. Qiao and Z. J. Xu, *Chem. Soc. Rev.*, 2019, **48**, 2518–2534.
59 C. C. L. McCrory, S. Jung, J. C. Peters and T. F. Jaramillo, *J. Am. Chem. Soc.*, 2013, **135**, 16977–16987.
60 M. B. Stevens, L. J. Enman, A. S. Batchellor, M. R. Cosby, A. E. Vise, C. D. M. Trang and S. W. Boettcher, *Chem. Mater.*, 2017, **29**, 120–140.
61 Z. Wu, X. F. Lu, S. Zang and X. W. (David) Lou, *Adv. Funct. Mater.*, 2020, **30**, 1910274.
62 F. Zheng, Z. Zhang, D. Xiang, P. Li, C. Du, Z. Zhuang, X. Li and W. Chen, *J. Colloid Interface Sci.*, 2019, **555**, 541–547.
63 A. C. Lazanas and M. I. Prodromidis, *ACS Meas. Sci. Au*, 2023, **3**, 162–193.
64 R. Liu, G. Chen, Y. Guo, T. Li, J. Qiu, B. He and P. Tang, *Chem. Eng. J.*, 2024, **500**, 157098.
65 R. L. Doyle and M. E. G. Lyons, *Phys. Chem. Chem. Phys.*, 2013, **15**, 13737–13783.
66 G.-F. Li, M. Divinagracia, M. F. Labata, J. D. Ocon and P.-Y. Abel Chuang, *ACS Appl. Mater. Interfaces*, 2019, **11**, 33748–33758.
67 X. Li, Z. Zhang, X. Zhuang, Z. Jia and T. Wang, *Chin. J. Chem.*, 2024, **42**, 3533–3552.
68 Y. Hao, X. Cao, C. Lei, Z. Chen, X. Yang and M. Gong, *Mater. Today Catal.*, 2023, **2**, 100012.
69 F. Dionigi and P. Strasser, *Adv. Energy Mater.*, 2016, **6**, 1600621.

